https://doi.org/10.5194/amt-2020-407
Preprint. Discussion started: 20 October 2020

Atmospheric Measurement Techniques Discussions

A study of polarimetric noise induced by satellite motion: Application to the 3MI and similar sensors

Souichiro Hioki[1], Jérôme Riedi[1], Mohamed S. Djellali[1]

[1] Univ. Lille, CNRS, UMR 8518 - LOA - Laboratoire d'Optique Atmosphérique, Lille, F-59000, France

Correspondence to: Souichiro Hioki (souichiro.hioki@univ-lille.fr)

Abstract. This study investigates the magnitude of the noise introduced by the co-registration and interpolation in computing Stokes vector elements from observations by the Multi-viewing, Multi-channel, Multi-polarisation Imager (3MI). The 2-D polarimetric measurements from the Second-Generation Global Imager (SGLI) are weighted and averaged to produce two proxy datasets of the 3MI measurements, with and without considering the effect of the satellite motion along the orbit. By comparing these two datasets, we estimate the magnitude of the noise introduced by co-registration and interpolation that are necessary to offset the satellite's motion along the orbit. The results show that the noise is not symmetric about zero and not negligible when the intensity variability of the observed scene is large. The results are analyzed in four categories of pixels, and the most spread distribution of normalized polarized radiance difference is in the cloud-over-water category with the 5th to 95th percentile range being [-0.0051:-0.012]. The most spread distribution of degree of linear polarization difference is for the coastline category with the same percentile range being [-0.019:0.082]. A model using Monte Carlo simulation confirms that the magnitude of these errors over clouds are closely related to the spatial correlation in the horizontal cloud structure. For the cloud-over-water category, it is shown that the noise model developed in this study can statistically predict the magnitude and trends of the 3MI noise estimated from SGLI data. The obtained statistics and the simulation technique can be utilized to provide pixel-level quality information for 3MI Level 1B products. In addition, the simulation method can be applied to the past, current, and future spaceborne instruments with a similar design.

1. Introduction

The Multi-viewing, Multi-channel, Multi-polarisation Imager (3MI) is a planned spaceborne sensor on the MetOp Second Generation-A (MetOp-SG-A) satellite platform. The sensor consists of two wide field-of-view cameras with narrow-band wavelength filters, inheriting the legacy of the Polarisation and Directionality of the Earth's Reflectance (POLDER) sensor. The rotating wheel carries 31 filters that enable polarimetric measurements at 9 wavelengths and non-polarimetric measurements at 3 wavelengths (Fougnie et al. 2018). The spatial resolution at nadir is 4 km and the instantaneous swath is 2200 km. The MetOp-SG-A series expects the launch of three identical platforms with seven-year intervals, providing continuous and homogeneous monitoring of the Earth's weather and climate for 21 years. The 3MI sensors on these platforms

https://doi.org/10.5194/amt-2020-407
Preprint. Discussion started: 20 October 2020


Atmospheric Measurement Techniques Discussions

are anticipated to perform multi-viewing and multi-channel polarimetric observation at unparalleled spatial and temporal scales.

As increasingly advanced retrieval techniques are used to extract atmospheric composition parameters from multispectral and polarimetric observations (Knobelspiesse et al. 2012; Fu and Hasekamp 2018; Dubovik et al. 2019), the knowledge and reduction of uncertainties associated to polarimetric measurements become more and more critical. In particular for all techniques relying on optimal estimation, the correct understanding of observational uncertainties, as discussed in details by Povey and Grainger (2015), is pivotal to obtain meaningful and successful retrieval. With no onboard calibration, the 3MI sensor needs to rely on inflight vicarious calibration techniques to monitor and assess the instrument radiometric performances. In addition to several existing methods (Fougnie, 2016), new techniques are being developed to improve the 3MI calibration (Djellali et al., 2019) and synergies with other sensors of the METOP-SG A platform will also be beneficial (Fougnie et al., 2018).

The radiometric performance of the instrument however is not the only factor driving the overall measurement uncertainties especially for polarimetric observations where the useful quantities (Stokes parameters) are not directly measured but derived, for example, from a set of different radiances. Therefore, the polarimetric performance of the 3MI instrument will depend both on the radiometric accuracy and the process used to derive the Stokes parameters. This paper investigates in particular the uncertainty induced by this derivation process in order to provide instantaneous, realistic, and quantitative estimate of polarization noise at pixel level for the 3MI instrument or similar sensors.

The 3MI instrument derives the first three Stokes parameters (I, Q, and U) by synthesizing three wide-field-of-view images that are taken sequentially at 0.25 seconds interval. Each of three images is acquired with linear polarizer oriented in different directions with polarizing axis being -60°, 0° and 60° with respect to the direction of the satellite's orbital motion (along-track direction). However, within the 0.25-second interval, the instantaneous field of view (IFOV) shifts by 1.8 km on the ground because of the motion of the satellite. The shifts between the acquired images lead to the need for the interpolation and co-registration to compensate the satellite's along-track motion before the computation of the Stokes parameters. These non-simultaneous acquisitions therefore introduce a possible source of noise in the polarimetric observation by the 3MI sensor due the co-registration and the interpolation required to match the three images.

The magnitude of noise due to the interpolation and co-registration is expected to be neither spatially uniform nor symmetric about zero, and therefore cannot be removed by spatio-temporal averaging. This is because the intensity in the original images and the polarized normalized radiance (L_p) are not linearly related. We define the normalized radiance (L) and, in analogy, the polarized normalized radiance as follows:

$$L = \frac{\pi I}{E_0} \quad (1)$$

$$L_p = \frac{\pi}{E_0}\sqrt{Q_i^2 + U_i^2}, \quad (2)$$

where I is the intensity, Q_i and U_i are the second and third elements of Stokes vector in terms of intensity, E_0 is the beam flux of the extraterrestrial solar radiation. The degree of linear polarization (DOLP) is defined as follows:

https://doi.org/10.5194/amt-2020-407
Preprint. Discussion started: 20 October 2020


Atmospheric Measurement Techniques Discussions

$$\mathrm{DOLP} = \frac{L_p}{L}. \quad (3)$$

Assuming three ideal polarizers with a perfect alignment, the normalized radiance and the polarized normalized radiance can be computed from the original intensity measurements (X_{m60}, X_0, X_{p60}) as follows:

$$L = \frac{2}{3}\frac{\pi}{E_0}\left(X_{m60} + X_0 + X_{p60}\right) \quad (4)$$

$$L_p = \frac{2\sqrt{2}}{3}\frac{\pi}{E_0}\sqrt{(X_{m60} - X_0)^2 + \left(X_0 - X_{p60}\right)^2 + \left(X_{p60} - X_0\right)^2}, \quad (5)$$

where X_{m60} corresponds to the intensity with the polarizer aligned -60° off from the along-track direction, X_0 to 0° off, and X_{p60} to +60° off. Equation (5) demonstrates that the noise in the original images and the normalized polarized radiance are not in linear relation. Rather, the noise tends to suppress the polarization for strongly polarized target and tends to enhance the polarization for weakly polarized target. As the quality of the retrieval product hinges on the quality of the radiance product and ancillary information that delivers the reliability, the quantification of the noise triggered by the interpolation and co-registration is significantly useful in the quality control of both Level 1B and Level 2 data products.

Section 2 describes the data and methods used in this study, Section 3 the results, and Section 4 the discussion on the simulation of the noise statistics. Conclusions are given in Section 5.

2. Data and methods

2.1 Data

In this study, we produce 3MI proxy polarimetric measurements from the actual high-resolution polarimetric measurements obtained by the Second-Generation Global Imager (SGLI) aboard the Global Change Observation Mission – Climate (GCOM-C) satellite (Imaoka et al. 2010). The SGLI sensor provides polarized normalized radiances at 1 km nadir resolution within a 1150 km-wide swath. As the SGLI is a push-broom sensor, the interpolation noise is expected to be negligible compared to that introduced by the 3MI's more complex co-registration and interpolation. We treat the SGLI measurement as truth and evaluate the magnitude of noise introduced by the interpolation and co-registration by producing 3MI-proxy data. One week of global SGLI Level 1B data near the 2008 September equinox (September 20-26) is used. As the GCOM-C satellite is in the sun-synchronous orbit at 800 km altitude with descending-node local time of 10:30, the data from the SGLI is valuable to simulate measurements from the 3MI that is anticipated also in the sun-synchronous morning orbit at 830 km altitude.

2.2 Methods

2.2.1 Estimation of the noise

As the nominal resolution of the 3MI is 4 km and that of the SGLI is 1 km, 4 × 4 SGLI pixels are aggregated to produce a 3MI pixel. We repeat the aggregation for every 4 × 4 SGLI pixel blocks in three original ("Lt_P2_m60", "Lt_P2_0", and

https://doi.org/10.5194/amt-2020-407
Preprint. Discussion started: 20 October 2020


Atmospheric Measurement Techniques Discussions

"Lt_P2_p60") radiance data in the SGLI Level 1B product. These three datasets correspond to the radiance measured at 0.869 μm with polarizers at three different directions at -60°, 0°, and 60° with respect to the along-track axis of the satellite (i.e., X_{m60}, X_0, X_{p60}). From the aggregated data, we compute the normalized radiance and polarized normalized radiance by Eqs. (4) and (5). The results are referred to as "reference data" hereafter.

A similar method is applied to produce the 3MI "proxy data" which is compared to the reference data to estimate the magnitude of the noise. The proxy data is different from the reference data in that it incorporates the effects of satellite's motion and interpolation. To simulate the motion of satellite between the acquisition of each image (1.8 km), we compute the contribution of every SGLI pixel to the shifted 4×4 grid as in Table 1. The contribution factors are multiplied to the measured radiance in every SGLI pixel to perform the weighted average. After computing the weighted average, we obtain the shifted, aggregated images of "Lt_P2_p60" and "Lt_P2_m60" from which unshifted (with respect to the "Lt_P2_0" image) aggregated images are produced by linear interpolation. The linear interpolation is selected for the simplicity and the locality, but the noise estimation described in this subsection as well as the noise simulation detailed in Subsection 2.2.3 could be performed with other methods of interpolations if deemed necessary for specific applications. The final contribution factors are summarized in Table 2. From these unshifted aggregated images, we compute the normalized radiance (L) and the normalized polarized radiance (L_p) by Eqs. (4) and (5), and call it the "proxy data".

The comparison of the proxy and reference data is performed on a pixel-by-pixel basis. In every pixel, the difference of polarized normalized radiance ΔL_p and the difference of degree of linear polarization ΔDOLP are computed. These differences are attributed to the noise induced by the pixel co-registration and the interpolation.

2.2.2 Stratification of data

To further the analysis of the noise, we classify pixels into four categories: coastlines, clear sky over land, clouds over land, and clouds over water. The classification is based on the land-water flag in the SGLI Level 1B dataset and the cloud flag algorithm developed for this study. The activity diagram (flow-chart) of the cloud flag algorithm is shown in Fig. 1 while individual test conditions are listed in Tables 3 (pixels over water) and 4 (pixels over land). To compute cloud flag in the SGLI Level 1B POLDK product's coordinate, other SGLI L1B products (VNRDK, VNRDL, IRSDK, and IRSDL products) are projected onto the POLDK grid. Once the cloud flag is derived, both land-water flag and cloud flag are extended into the along-track directions by 20 SGLI pixels to cover all SGLI pixels used for the noise estimation and to minimize the pixels on boundaries. A pixel is classified as "clear-sky over land" when it is flagged as "confidently clear" and "land cover 100%", "cloud over land" when it is flagged as "confidently cloudy" and "land cover 100%", "cloud over water" when "confidently cloudy" and "land cover 0%", and "coastline" when land cover is between 5% and 95%. Only pixels with glint angle greater than 35° are collected for coastlines and cloud-over-water classes to avoid contamination by sun glints.

In every class of data, the aforementioned differences (ΔL_p and $\Delta DOLP$) are stratified by the along-track Laplacian that is defined as follows:

https://doi.org/10.5194/amt-2020-407
Preprint. Discussion started: 20 October 2020


Atmospheric Measurement Techniques Discussions

$$L_{AT} = \frac{\pi}{E_0}(2X_0 - X_{-1} - X_{+1}), \quad (6)$$

where X_{-1} is the X_0 of the adjacent pixel in the negative along-track direction, and X_{+1} is the X_0 of the adjacent pixel in the positive along-track direction. The along-track Laplacian is a measure of the non-linearity of the local intensity change in the along-track direction. We select this metric because we expect that the major source of the noise is the spatial inhomogeneity of the total radiance that propagate through the linear interpolation performed in the co-registration.

2.2.3 Prediction of noise

Alongside the noise estimation from the SGLI Level 1B data, the statistics of the noise is predicted with a Monte-Carlo model for pixels in cloud-over-water class. We generate synthetic 2-D normalized radiance fields by the inverse 2-D Fourier transform, assuming the power-low spectrum of the normalized radiance distribution. We then proceed through with the weighting and aggregation equivalent to the method described in Section 2.1. This process is repeated for 10 million samples to realize meaningful statistics. The details of the method are described in the rest of this subsection.

The first step is to apply inverse 2-D Fourier transform to the assumed power-law spectrum with Gaussian noise as in the method described by Iwabuchi and Hayasaka (2002). A number of studies show that the intensity spectrum of the cloud field follows the power-law (Cahalan and Snider 1989, Davis et al. 1997, Marshak et al. 1995, 1998, Oreopoulos et al. 2000) and the slope is known to be a function of horizontal spatial scale. For the scale greater than a few hundred meters and less than a few hundred kilometers, the power-law coefficient is between -1.5 and -2.0, and the value increases for the smaller. We select $-5/3$ $(1.666\cdots)$ as the power-law coefficient in our simulation.

Every synthetic 2-D normalized radiance field that is generated in this way are different. They are however statistically centered at zero, and their variance depends on the prescribed power-law coefficient. In the second step, to make the simulation consistent with the SGLI-based estimation, we scale and add offset to each realization as in the following equation:

$$L_{(i,j)} = ax_{(i,j)} + b, \quad (7)$$

where $L_{(i,j)}$ is the final 2-D normalized radiance field, $x_{(i,j)}$ the output of the inverse Fourier transform, a the scaling coefficient and b the offset. The scale a and offset b are determined so that the pixel intensity $\bar{L} = \sum_i w_i L_i$ and weighted variance $V = \sum_i w_i (L_i - \bar{L})^2$ follow the observed empirical distribution function (EDF) of normalized radiance $\hat{F}_L(l)$ and weighted variance $\hat{F}_V(v; l)$. These EDFs are computed from the SGLI data upon performing the noise estimation described in Section 2.1. The EDF of variance $\hat{F}_V(v; l)$ is computed for each small normalized radiance interval, spanning from 0 to 0.9 with 0.01 width, from 0.9 to 1 with 0.05 width, and from 1 to 1.5 with 0.5 width. The weight w_i is the arithmetic mean of final weights in Table 2 for every line (i.e. for Line 5, it is 1/16 + 9/320 + 11/320 =1/240).

The third step is to compute $X_{1(i,j)}$, $X_{2(i,j)}$, and $X_{3(i,j)}$ from the 2-D normalized radiance field $L_{(i,j)}$, the angle of linear polarization (AOLP) χ, and the degree of linear polarization (DOLP) δ. The AOLP are sampled so that it follows the EDF of AOLP $\hat{F}_\alpha(\alpha; l)$, and the DOLP are sampled so that it follows EDF of DOLP $\hat{F}_\delta(\delta; l)$. The AOLP is assumed constant over subpixels for each realization, but the DOLP is sampled for each subpixel because of the strong intensity-dependence with

https://doi.org/10.5194/amt-2020-407
Preprint. Discussion started: 20 October 2020


Atmospheric Measurement Techniques Discussions

weak spatial correlation. Figure 2 shows the strong decreasing trend of the DOLP with intensity. We note here that the statistics of the intensity-stratified DOLP and the statistics of AOLP have been found necessary for the reasonable simulation of the polarimetric noise. This is presumably because the DOLP varies significantly as a function of reflectivity at cloud boundaries and over thin clouds, and the AOLP determines the relative contribution of noise in X_1 and X_3 images to the polarized normalized radiance (L_p).

Once $X_{1(i,j)}$, $X_{2(i,j)}$, and $X_{3(i,j)}$ are obtained, the last step is to proceed through with the weighting and aggregation equivalent to the method described in Section 2.1. This entire process of 2-D Fourier transform, scaling, and X_1-X_2-X_3 derivation is repeated 10 million times.

3. Results

3.1 Evaluation of the noise

The difference of DOLP between the proxy and reference data is shown in Fig. 3 (a) with corresponding visible composite in Fig. 3 (b). The figure covers the western French coast, English Channel, and the southern Great Britain island. Figure 3 (a) shows that the DOLP difference can reach close to 0.4 along the coastlines, particularly in a part where the coastline runs in the cross-track direction. There is little negative DOLP difference near positive values, implying that the distribution of the DOLP difference is not symmetric about zero. Along the edges of thin clouds, for example over the Atlantic in the western part of the Fig. 3, positive and negative DOLP differences are mixed. The magnitude of the noise is smaller over thick clouds covering the eastern end of English Channel than along coastlines. Figure 3 demonstrates that the magnitude of noise introduced by the interpolation is not negligible over the scene where intensity variation is large.

It is not only over coastlines that the distribution of noise is asymmetric about zero. In Figs. 4 and 5, we show histograms of degree of linear polarization (DOLP) and polarized normalized radiance (L_p) differences for four different classes of pixels defined in Sect. 2.2.2: coastlines, clear sky over land, clouds over land, and clouds over water. Figures 4 and 5 show that the distributions of the proxy-reference differences are not symmetric about zero and rather skewed to the right (having fat tail in the right end of the histogram) in all classes of data. The tail of DOLP difference histogram is particularly fat for cloud-over-water and coastlines classes, where sharp reflectance gaps near coastal water or cloud edges induce strong polarization artifact. The asymmetry can be confirmed from the 5th to 95th percentile range and 25th to 75th percentile range (interquartile range) of the estimated DOLP and L_p noise as presented in Table 5. The coastlines class has the most spread distribution of DOLP differences, and the 5th-95th percental range is $[-0.019: 0.082]$. On the other hand, the cloud-over-water class has the most spread distribution of L_p differences, and the 5th to 95th percentile range is $[-0.0051: 0.012]$. The asymmetry of the distribution implies that the noise cannot be completely cancelled out by computing the spatial average.

Figure 6 shows the proxy-reference differences stratified by the along-track Laplacian (L_{AT}). As the L_{AT} increases, the median of the noise as well as the spread increase. For clouds over land and clouds over water, the spreads of the distributions saturate

https://doi.org/10.5194/amt-2020-407
Preprint. Discussion started: 20 October 2020


Atmospheric Measurement Techniques Discussions

when L_{AT}/L increases, while for coastlines the spread of the distribution does not saturate. In the clear-sky-over-land class, the spread reaches a peak at $L_{AT}/L = 0.15$. Good stratifications by the along-track Laplacian shown in this study imply that the magnitude of the noise is predictable from the image of X_0 (intensity with polarizer at 0° off the along track direction), which is used to compute the L_{AT} and observationally available.

The distribution of polarized normalized radiance difference (L_p difference) is also stratified well by the along-track Laplacian (L_{AT}), and Fig. 7 show the increase of median with increasing L_p. In similar way as for the DOLP difference, the spreads of distributions for cloudy classes saturate at about $L_{AT} = 0.1$, whereas it does not for the coastlines class. The spread for the clear-sky pixels over land does not show a maximum as seen in the distribution of the DOLP differences.

A straightforward implication of the clear stratification is that it is possible to predict the quality of polarization data in every pixel. For example, the median bias and the standard deviation can be estimated for every pixel because they are computable from the obtained statistics and observed X_0 (and derived L_{AT}) value. Such information would prove useful for the quality control of retrieval products as well as data assimilation or any retrieval algorithm requiring pixel level uncertainty estimates.

3.2 Prediction of noise

Figure 8 shows the predicted magnitude of noise based on the Monte Carlo simulation for cloudy pixels over water. The simulation predicts the median (red curves) that matches well to the estimation based on the SGLI data (dotted curves). As the empirical 95th percentile of the L_{AT}/L is 0.39 and that of L_{AT} is 0.070, the abscissas of Fig. 8 cover the large portion of the plausible range of the data. A slight overestimation of the DOLP difference occurs in the entire range, but the maximum difference is 0.0010 (i.e. 2.2%) in the bin $0.36 < L_{AT}/L < 0.365$. The difference between the predicted and estimated normalized polarized radiance is less than 10^{-3} in $L_{AT} < 0.12$. The difference reaches 1.5×10^{-3} (i.e. 5.4%) in the bin $0.16 < L_{AT} < 0.17$. Overall, the simulation can predict the median of the noise estimation at better than 5% accuracy.

The successful prediction of the noise by the statistical model implies that the noise distribution in the cloud-over-water class inferred from the SGLI data is a result of the inherent horizontal structure of clouds. The method is likely be applicable to other spatial scale to predict the magnitude of noise of the past, current, and future polarimetric instruments sharing similar designs. In the application to other satellite data, it is necessary to collect the several statistics that are used in the simulation, namely, normalized radiance distribution, normalized-radiance-stratified sub-pixel inhomogeneity (weighted variance), normalized-radiance-stratified DOLP, and normalized-radiance-stratified AOLP. However, most of these statistics are readily available from observations (past and current sensors) or simulations (future sensors). The exception is the sub-pixel inhomogeneity that may be a challenging parameter to obtain if a past or current sensor has no collocated high-resolution imaging measurements, but one could replace it with an alternative measure of the local inhomogeneity, for example, the variance of X_0 in the along-track direction. The modeling technique in this work is therefore particularly helpful for the preparation for future missions.

https://doi.org/10.5194/amt-2020-407
Preprint. Discussion started: 20 October 2020


Atmospheric Measurement Techniques Discussions

4. Discussions

In this study, our simulation of the noise statistics assumes power-law coefficient $(-5/3)$, but it is known that the power-law coefficient varies depending on type of clouds and spatial scale. A well-known example is for the scale break that occurs in the Landsat radiance data over stratocumulus clouds. When the spatial scale is less than a few hundred meters, the power law coefficient becomes significantly smaller (i.e. the spectrum becomes steeper). Smaller power-law coefficient means that low-frequency structures pronounce more than high frequency structures. As a result, when a lower power-law coefficient is specified, the simulated 2-D normalized radiance field looks more horizontally homogeneous, introducing smaller noise in simulated 3MI polarimetric measurements.

To test the sensitivity of our prediction to the specified power-law coefficient, we simulate the noise statistics for two other extreme cases. Figure 8 shows the stratified magnitude of noise in the DOLP and L_p when no correlation between neighboring subpixel is assumed, and Fig. 9 when smaller power-law coefficient (-3.0) is assumed.

When there is no spatial correlation in the cloud intensity, the magnitude of simulated noise is larger than the estimates based on the SGLI data. The median of SGLI-based estimate is out of the interquartile range of the simulation (gray shading in Fig. 8) for a significant range of L_{AT}/L and L_{AT}. On the other hand, Fig. 9 shows that the magnitude of simulated noise is slightly lower when smaller power-law coefficient (-3.0) is assumed. In addition, we note that the SGLI noise estimation for the clouds-over-land category also shows the slope between these two extremes.

From these results, we propose that the spatial correlation of intensity due to the natural cloud structure should be considered when predicting the statistics of noise over clouds. For the 3MI sensor, the higher resolution observations provided by the VII sensor (Wallner et al, 2017) aboard the same METOP-SG A platform might be used to further constrain the along track scene spatial correlation and therefore useful to improve the pixel-level polarimetric uncertainty estimates.

5. Conclusions

From the high-resolution global polarimetric observation by the SGLI, we estimate the 3MI's polarimetric noise induced by the co-registration and interpolation that compensates satellite's along-track motion during the acquisition. The estimates show that the magnitude of the noise introduced by interpolation is not negligible or asymmetric about the zero particularly over the locations where intensity variation is large.

The asymmetric distribution of the noise is confirmed in all four categories of analyzed pixels: clear-sky over land, clouds over land, clouds over water, and coastlines. The coastlines category had the most spread distribution of the degree of linear polarization (DOLP) difference, whereas the cloud-over-water class had the most spread distribution of the polarized normalized difference (L_p) differences. The 9th to 95th percentile range was $[-0.019: 0.082]$ for the DOLP differences and $[-0.0051: 0.012]$ for the L_p differences. These differences are well stratified by the along-track Laplacian that characterizes the non-linear change of the normalized radiance (L_p difference), or that divided by the normalized radiance (DOLP

https://doi.org/10.5194/amt-2020-407
Preprint. Discussion started: 20 October 2020


Atmospheric Measurement Techniques Discussions

difference). As the along-track Laplacian is available from the observation, a pixel-level quality information can be obtained based on the statistics presented in this study. In addition, it is possible to perform the statistical estimation of noise when the sub-pixel inhomogeneity is available as an input. Either procedures proposed in this study would help ensure the reliability of the radiance products and downstream applications including retrieval products as well as data assimilation.

The noise statistics based on the SGLI data and Monte Carlo simulation agree within 5% in terms of median bias, implying the predictability of the noise for cloudy pixels at an arbitrary spatial scale. The sensitivity study on the assumed power-law coefficient proved the need for the spatial correlation to be included in the noise prediction. The method of prediction is applicable to past, current and future missions with a polarimetric instrument based on a similar design, paving a way to better predict the performance of the instrument on orbit at the stage of planning. Finally, although simulations presented here are limited to cloudy scenes, similar diagnosis might be made for land surfaces under clear sky conditions for use in aerosol remote sensing applications.

Data availability

GCOM-C/SGLI data used in this study is available from the G-Portal website (https://gportal.jaxa.jp/gpr/) by Japan Aerospace Exploration Agency (JAXA).

Author contributions

Souichiro Hioki and Jérôme Riedi conceived of the methodology and outlined the project. Souichiro Hioki performed the study and composed the manuscript. Jérôme Riedi encouraged and supervised the project. Mohamed S. Djellali contributed the research activities through discussions on the results.

Competing interests

The authors declare that they have no conflict of interest.

Acknowledgements

We appreciate Japan Aerospace Exploration Agency (JAXA) for providing the GCOM-C/SGLI data needed for the research. This research is conducted in a framework of jointly-funded postdoctoral fellowship by Centre National d'Études Spatiales (CNES) and the Make Our Planet Great Again (MOPGA) program by Campus France. The authors are grateful for the financial support and various encouragements by CNES, MOPGA, and the Laboratoire d'Optique Atmosphérique.

https://doi.org/10.5194/amt-2020-407
Preprint. Discussion started: 20 October 2020


Atmospheric Measurement Techniques Discussions

References

Cahalan, R. F., and Snider, J. B.: Marine stratocumulus structure, Remote Sens. Environ., 28, 95-107, doi=10.1016/0034-4257(89)90108-9, 1989.

Davis, A., Marshak, A., Cahalan, R., and Wiscombe, W.: The Landsat scale break in stratocumulus as a three-dimensional radiative transfer effect: Implications for cloud remote sensing, J. Atmos. Sci., 54, 241-260, doi=10.1175/1520-0469(1997)054<0241:TLSBIS>2.0.CO;2, 1997.

Djellali, M. S., Riedi, J., Marcq, S., Fougnie, B., Hioki, S., and Nicolas, J.-M.: Development of calibration methods using specular reflection over the ocean for the multiviewing, multichannel, multipolarization imager (3MI) of the Eumetsat polar system - second generation (EPS-SG), Proceedings of SPIE, 11155, Conference on Image and Signal Processing for Remote Sensing XXV, Strasbourg, FRANCE, Sep 09-11, 2019, doi=10.1117/12.2532501, 2019.

Dubovik, O., Li, Z., Mishchenko, M. I., Tanre, D., Karol, Y., Bojkov, B., Cairns, B., Diner, D. J., Espinosa, W. R., Goloub, P., Gu, X., Hasekamp, O., Hong, J., Hou, W., Knobelspiesse, K. D., Landgraf, J., Li, L., Litvinov, P., Liu, Y., Lopatin, A., Marbach, T., Maring, H., Martins, V., Meijer, Y., Milinevsky, G., Mukai, S., Parol, F., Qiao, Y., Remer, L., Rietjens, J., Sano, I., Stammes, P., Stamnes, S., Sun, X., Tabary, P., Travis, L. D., Waquet, F., Xu, F., Yan, C., and Yin, D.: Polarimetric remote sensing of atmospheric aerosols: Instruments, methodologies, results, and perspectives, J. Quant. Spectrosc. Radiat. Transf., 224, 474-511, doi=10.1016/j.jqsrt.2018.11.024, 2019.

Fougnie, B., Marbach, T., Lacan, A., Lang, R., Schluessel, P., Poli, G., Munro, R., and Couto, A. B.: The multi-viewing multi-channel multi-polarisation imager - Overview of the 3MI polarimetric mission for aerosol and cloud characterization, J. Quant. Spectrosc. Radiat. Transf., 219, 23-32, doi=10.1016/j.jqsrt.2018.07.008, 2018.

Fougnie, B.: Improvement of the PARASOL radiometric in-flight calibration based on synergy between various methods using natural targets, IEEE Trans. Geosci. Remote Sensing, 54, 2140-2152, doi=10.1109/TGRS.2015.2496322, 2016.

Fu, G., and Hasekamp, O.: Retrieval of aerosol microphysical and optical properties over land using a multimode approach, Atmos. Meas. Tech., 11, 6627-6650, doi=10.5194/amt-11-6627-2018, 2018.

Imaoka, K., Kachi, M., Fujii, H., Murakami, H., Hori, M., Ono, A., Igarashi, T., Nakagawa, K., Oki, T., Honda, Y., and Shimoda, H.: Global change observation mission (GCOM) for monitoring carbon, water cycles, and climate change, Proc. IEEE, 98, 717-734, doi=10.1109/JPROC.2009.2036869, 2010.

Iwabuchi, H., and Hayasaka, T.: Effects of cloud horizontal inhomogeneity on the optical thickness retrieved from moderate-resolution satellite data, J. Atmos. Sci., 59, 2227-2242, doi=10.1175/1520-0469(2002)059<2227:EOCHIO>2.0.CO;2, 2002.

Knobelspiesse, K., Cairns, B., Mishchenko, M., Chowdhary, J., Tsigaridis, K., van Diedenhoven, B., Martin, W., Ottaviani, M., and Alexandrov, M.: Analysis of fine-mode aerosol retrieval capabilities by different passive remote sensing instrument designs, Opt. Express, 20, 21457-21484, 2012.

Marshak, A., Davis, A., Wiscombe, W., and Cahalan, R.: Radiative smoothing in fractal clouds, J. Geophys. Res., 100, 26247-26261, doi=10.1029/95JD02895, 1995.

https://doi.org/10.5194/amt-2020-407
Preprint. Discussion started: 20 October 2020


Atmospheric Measurement Techniques Discussions

Marshak, A., Davis, A., Cahalan, R. F., and Wiscombe, W.: Nonlocal independent pixel approximation: Direct and inverse problems, IEEE Trans. Geosci. Remote Sensing, 36, 192-205, doi=10.1109/36.655329, 1998.

Oreopoulos, L., Marshak, A., Cahalan, R. F., and Wen, G. Y.: Cloud three-dimensional effects evidenced in Landsat spatial power spectra and autocorrelation functions, J. Geophys. Res., 105, 14777-14788, doi=10.1029/2000JD900153, 2000.

Povey, A. C., and Grainger, R. G.: Known and unknown unknowns: Uncertainty estimation in satellite remote sensing, Atmos. Meas. Tech., 8, 4699-4718, doi=10.5194/amt-8-4699-2015, 2015.

Wallner, O., Reinert, T., and Straif, C.: METIMAGE: A spectro-radiometer for the VII mission onboard METOP-SG, Proceedings of SPIE, 10562, International Conference on Space Optics, Biarritz, FRANCE, Oct 18-21, 2016, doi=10.1117/12.2296103, 2016.

https://doi.org/10.5194/amt-2020-407
Preprint. Discussion started: 20 October 2020

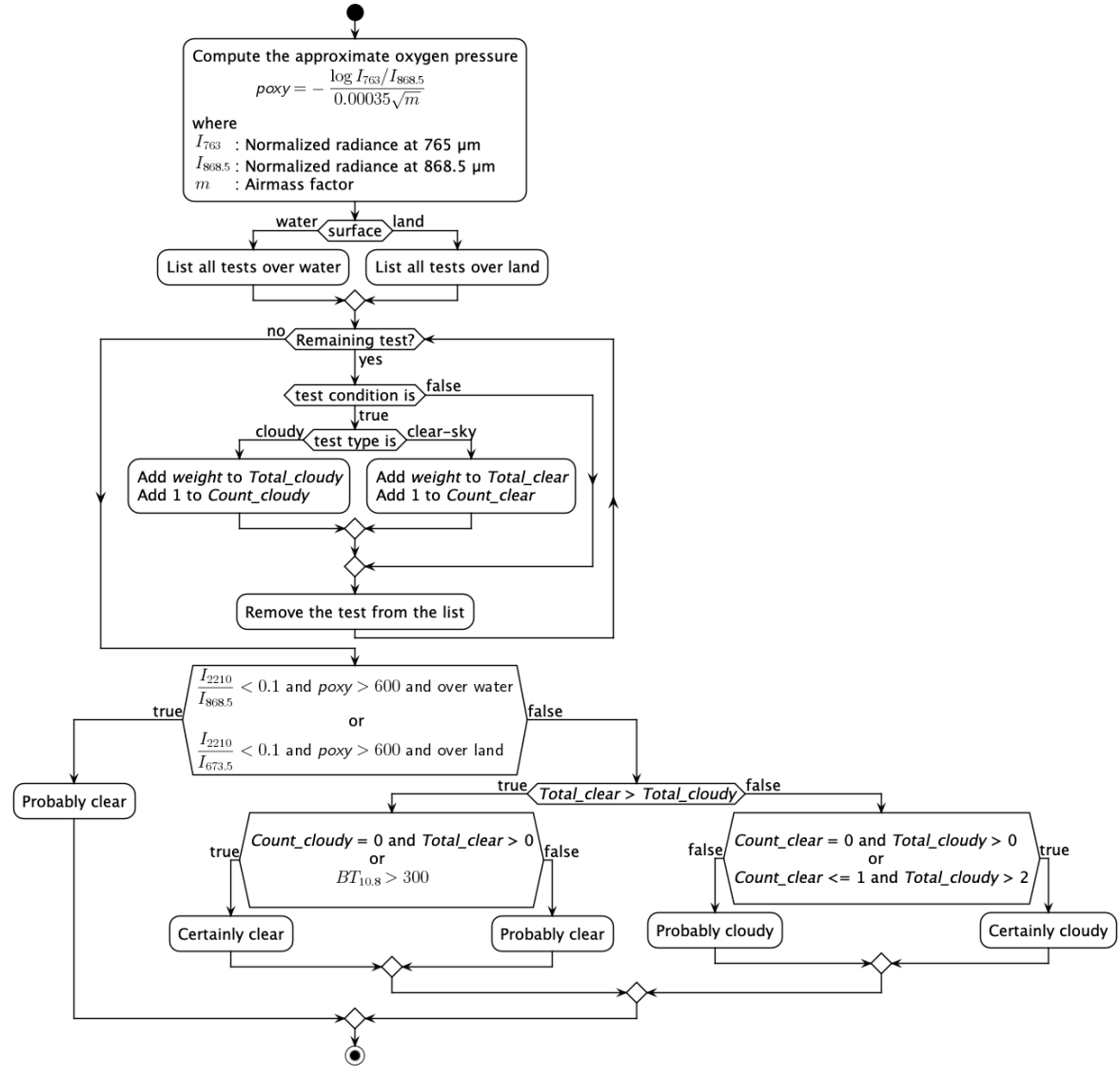

315 **Figure 1. The activity diagram (flow-chart) of the cloud-flag algorithm.**

https://doi.org/10.5194/amt-2020-407
Preprint. Discussion started: 20 October 2020

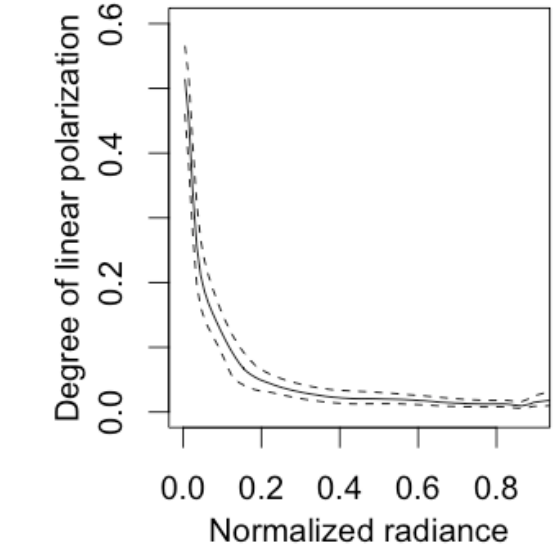

Figure 2. Decreasing trend of the degree of linear polarization for pixels over water with increasing intensity. The solid line is median, dashed lines are 25th and 75th percentile (interquartile range).

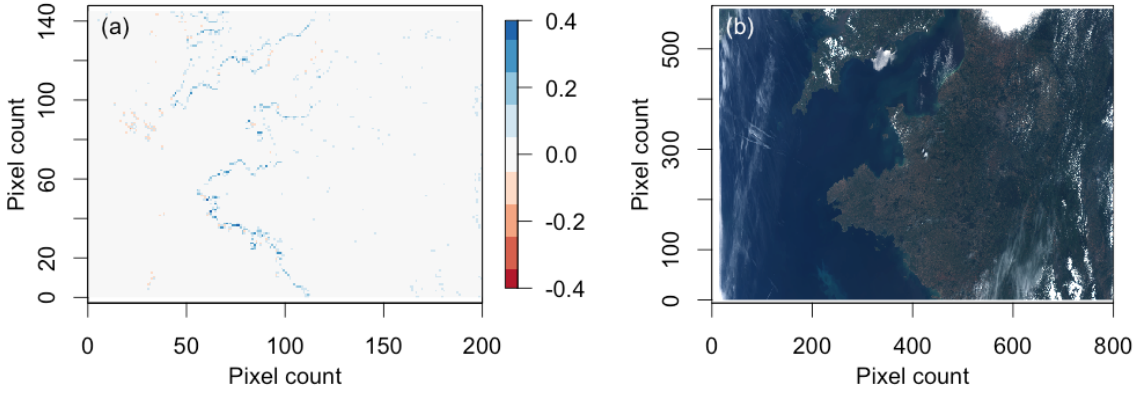

320 **Figure 3. (a) The DOLP difference between proxy and reference data. (b) The visible composite of the SGLI Level 1B data the same zone (visualized by authors, original data by JAXA).**

https://doi.org/10.5194/amt-2020-407
Preprint. Discussion started: 20 October 2020

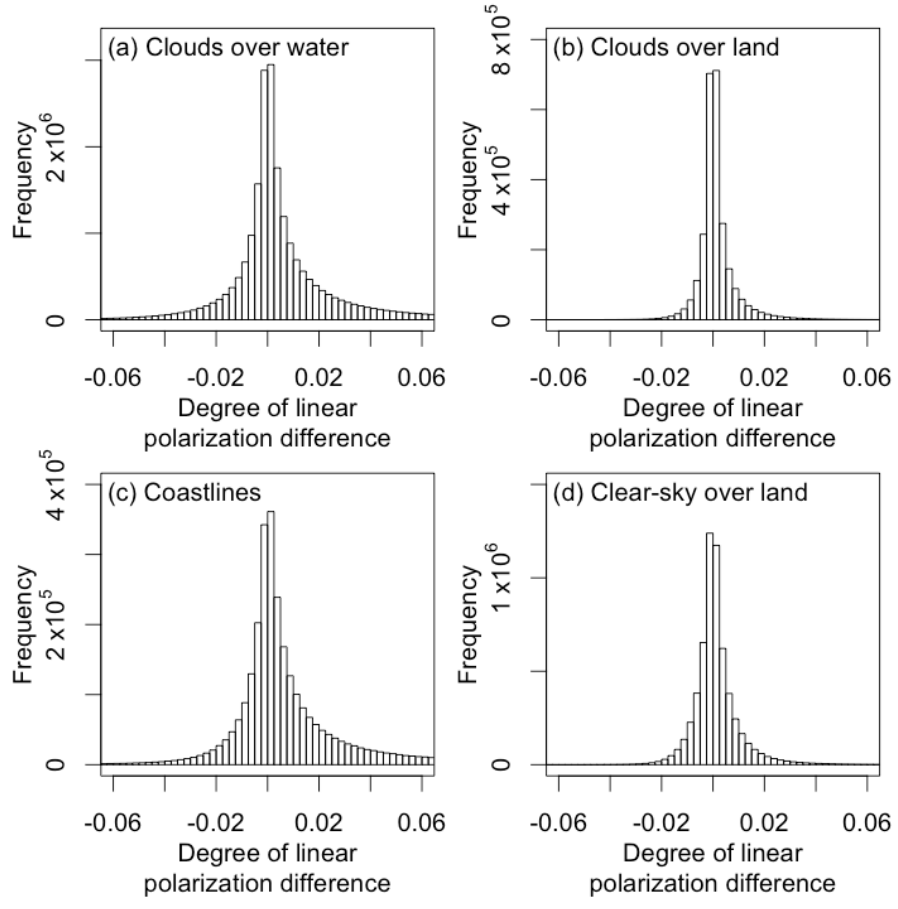

Figure 4. Histogram of proxy-reference differences in degree of linear polarization (DOLP) for (a) clouds over water, (b) clouds over land, (c) coastlines, and (d) clear-sky over land.

https://doi.org/10.5194/amt-2020-407
Preprint. Discussion started: 20 October 2020

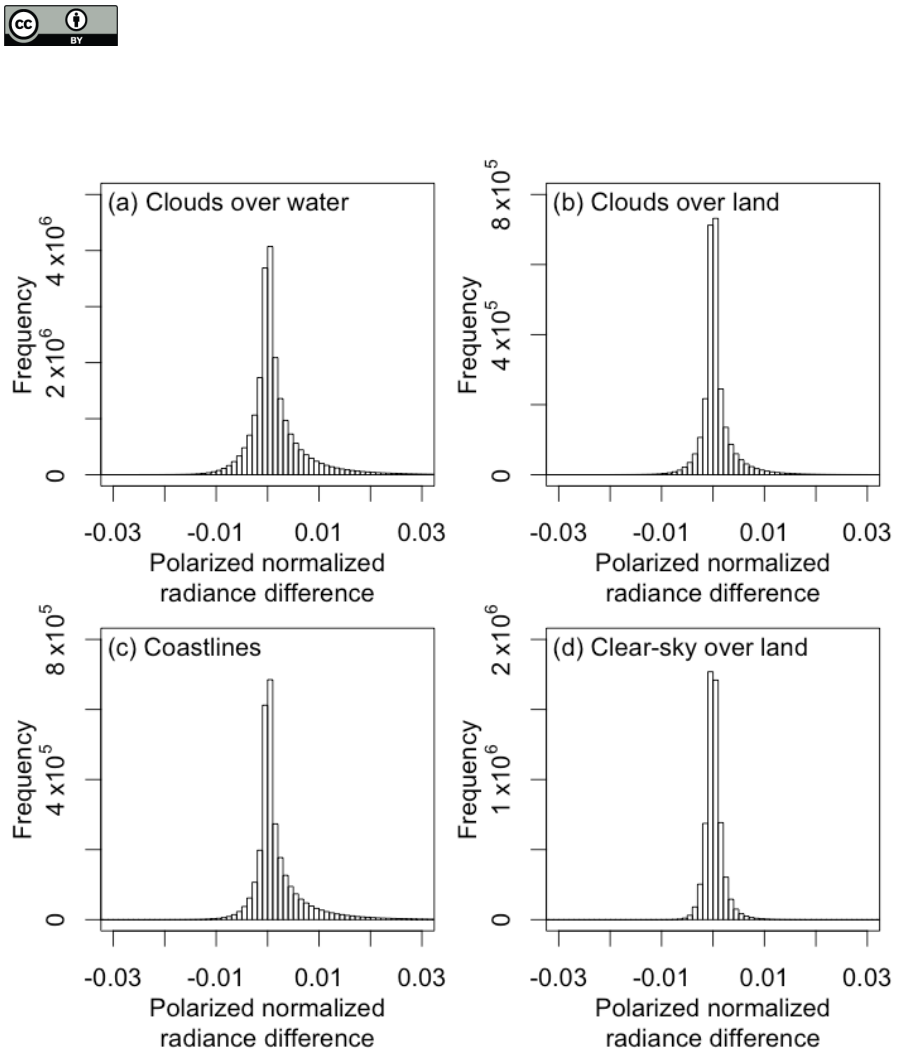

Figure 5. Histogram of proxy-reference differences in normalized radiance (*L*) for (a) clouds over water, (b) clouds over land, (c) coastlines, and (d) clear-sky over land.

https://doi.org/10.5194/amt-2020-407
Preprint. Discussion started: 20 October 2020

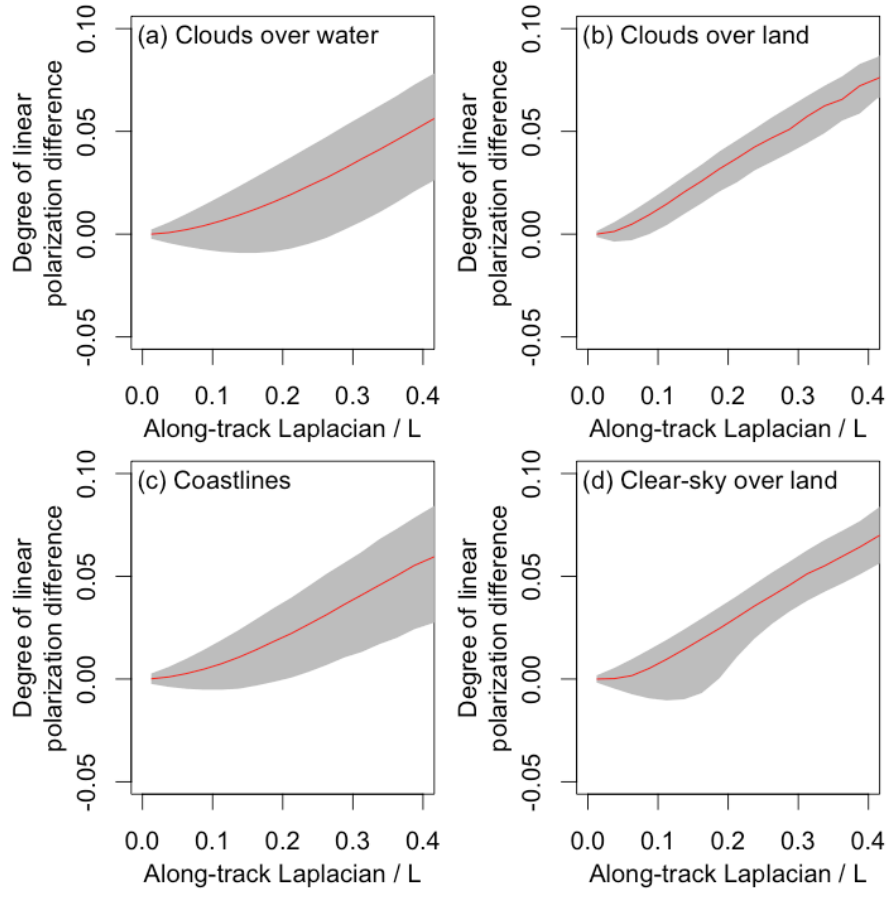

Figure 6. The proxy-reference differences in degree of linear polarization stratified by the along-track Laplacian divided by normalized radiance. Four panels are for: (a) clouds over water, (b) clouds over land, (c) coastlines, and (d) clear-sky over land. Red curves represent the median and gray shading indicate the interquartile range.

https://doi.org/10.5194/amt-2020-407
Preprint. Discussion started: 20 October 2020

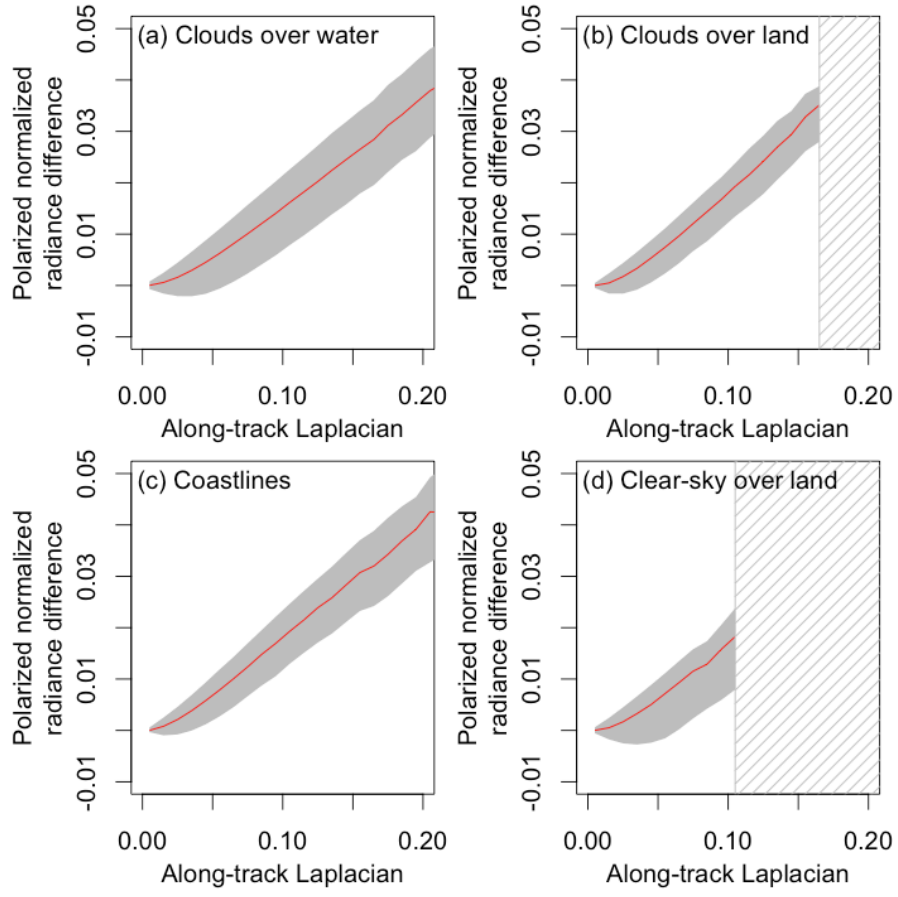

Figure 7. The proxy-reference differences in polarized normalized radiance stratified by the along-track Laplacian. Four panels are for: (a) clouds over water, (b) clouds over land, (c) coastlines, and (d) clear-sky over land. Red curves represent the median and gray shading indicate the interquartile range. Gray hatched area corresponds to the part where statistics is unavailable or unreliable because of limited number of data points.

https://doi.org/10.5194/amt-2020-407
Preprint. Discussion started: 20 October 2020

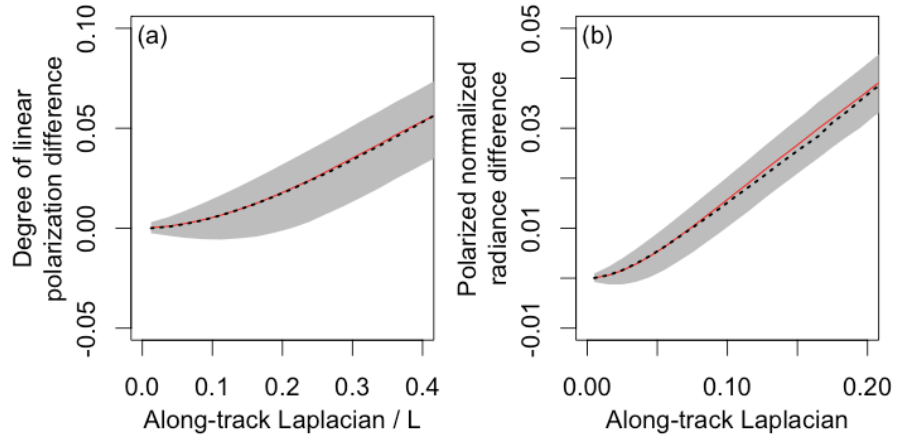

Figure 8. (a) The simulated proxy-reference difference in the degree of linear polarization stratified by the along-track Laplacian divided by normalized radiance (b) The simulated proxy-reference difference in the polarized normalized radiance stratified by the along-track Laplacian. Red curves represent median and gray shading indicate the interquartile range of the simulation. Black dotted curves correspond to the medians of the observation (i.e. Red curves in Figs. 6(a) and 7(a)).

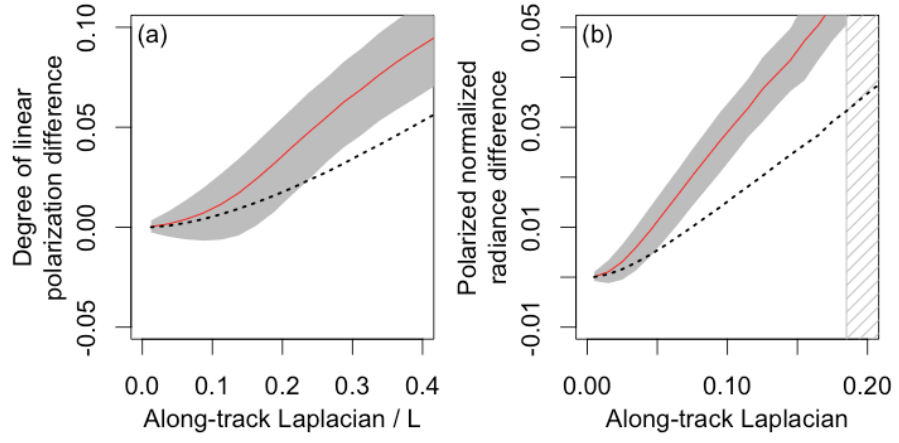

Figure 9. The same as Fig. 8 but without correlation in the cloud field simulation.

https://doi.org/10.5194/amt-2020-407
Preprint. Discussion started: 20 October 2020

Atmospheric Measurement Techniques Discussions

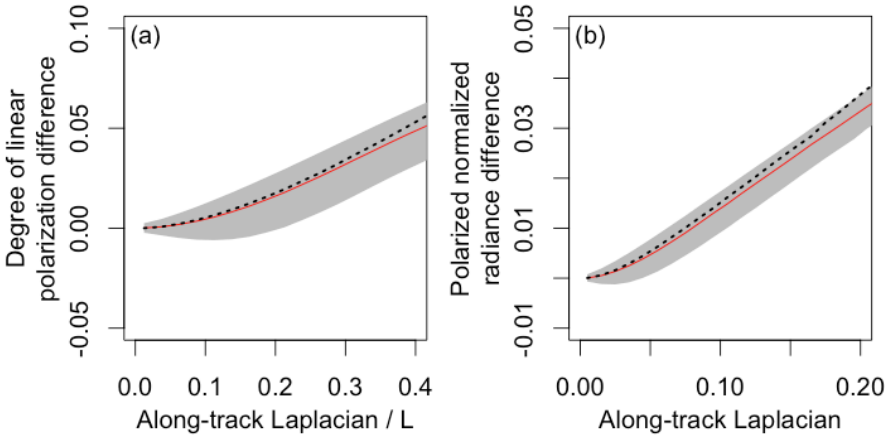

Figure 10. The same as Fig. 8 but with slope of -3.0

https://doi.org/10.5194/amt-2020-407
Preprint. Discussion started: 20 October 2020

Atmospheric Measurement Techniques Discussions

Table 1. Contribution of SGLI pixels to shifted and unshifted averaging grids for a single 3MI pixel. These weights are intended to simulate the along-track motion of the satellite.

Line	Weights for the unshifted grid	Weights for the shifted grid (+1.8 km)	Weights for the shifted grid (-1.8 km)
1	0	0	0
2	0	0	1/20
3	0	0	1/16
4	1/16	0	1/16
5	1/16	1/80	1/16
6	1/16	1/16	1/80
7	1/16	1/16	0
8	0	1/16	0
9	0	1/20	0
10	0	0	0

350

Table 2. Contribution of SGLI pixels to shifted and unshifted averaging grids for single 3MI pixel. These weights include the effects of satellite's along-track motion and the interpolation.

Line	Weights for the unshifted grid	Weights for the shifted grid (+1.8 km)	Weights for the shifted grid (-1.8 km)
1	0	0	0
2	0	9/1600	0
3	0	9/320	11/400
4	0	9/320	11/320
5	1/16	9/320	11/320
6	1/16	47/1600	11/320
7	1/16	11/320	47/1600
8	1/16	11/320	9/320
9	0	11/320	9/320
10	0	11/400	9/320
11	0	0	9/1600
12	0	0	0

https://doi.org/10.5194/amt-2020-407
Preprint. Discussion started: 20 October 2020

Atmospheric Measurement Techniques Discussions

355 **Table 3. Tests for the cloud detection algorithm over water. I_{XXX} indicates the normalized radiance at wavelength XXX nm, BT_{XX} the brightness temperature at XX µm, σ_{XXX} the standard deviation of I_{XXX} in the concentric box of 3 × 3 pixels.**

Test condition	Test type	Weight
$(I_{1630}/I_{868.5} < 1.2)$ and $(BT_{10.8} < 288\text{K})$ and $(I_{673.5} > 0.2)$	Cloudy	1
$I_{673.5} > 0.45$	Cloudy	10
$(I_{673.5} > 0.35)$ and $(\sigma_{673.5} > 0.01)$	Cloudy	10
$(I_{673.5} > 0.15)$ and $(1 < I_{673.5}/I_{868.5} < 1.1)$ and $(BT_{10.8} < 295\text{K})$	Cloudy	10
$(I_{673.5} > 0.2)$ and $(\sigma_{673.5} > 0.005)$ and $(I_{673.5}/I_{1630} < 1.4)$	Cloudy	100
$(BT_{10.8} - BT_{12} < -1\text{K})$ and $(BT_{10.8} < 300\text{K})$	Cloudy	1000
$(I_{1630}/I_{868.5} > 1.3)$ and $(BT_{10.8} > 300\text{K})$	Clear-sky	1
$(I_{673.5}/I_{868.5} < 0.7)$	Clear-sky	10
$(\sigma_{673.5} < 0.1)$ and $(0.2 < I_{673.5} < 0.5)$ and $(1.5 < I_{1630}/I_{673.5} < 10)$	Clear-sky	100
$I_{1630}/I_{673.5} > 2.2$	Clear-sky	100
$(BT_{10.8} - BT_{12})$ and $(BT_{10.8} > 300\text{K})$	Clear-sky	1000
$\left\lvert\frac{I_{868.5} - I_{673.5}}{I_{868.5} - I_{1630}}\right\rvert > 2$	Clear-sky	1000

Table 4. Tests for the cloud detection algorithm over land. The symbols are the same as in Table 3.

Test condition	Test type	Weight
$(I_{1630}/I_{868.5} < 1.2)$ and $(BT_{10.8} < 288\text{K})$ and $(I_{673.5} > 0.2)$	Cloudy	1
$(I_{868.5} > 0.1)$ or $(\sigma_{868.5} > 0.005)$	Cloudy	10
$I_{1630} > 0.1$	Cloudy	100
$(BT_{10.8} - BT_{12} < -1\text{K})$ and $(BT_{10.8} < 300\text{K})$	Cloudy	1000
$I_{1380} > 0.01$	Cloudy	1000
$(I_{1630}/I_{868.5} > 1.3)$ and $(BT_{10.8} > 300\text{K})$	Clear-sky	1
$(I_{673.5}/I_{868.5} < 0.7)$ and $(I_{868.5} < 0.05)$	Clear-sky	10
$0 < \sigma_{868.5}/I_{868.5} < 0.01$ and $I_{868.5} < 0.1$	Clear-sky	100

https://doi.org/10.5194/amt-2020-407
Preprint. Discussion started: 20 October 2020

Atmospheric Measurement Techniques Discussions

360 **Table 5. The intervals of degree of linear polarization difference (DOLP) and polarized normalized radiance (L_p) difference for percentiles that covers 90% and 50% of entire data.**

Percentile range	Pixel class	DOLP difference	L_p difference
[5th:95th]	Clear-sky over land	[-0.011:0.016]	[-0.0023:0.0032]
	Cloud over land	[-0.0075:0.014]	[-0.0033:0.0062]
	Cloud over water	[-0.023:0.060]	[-0.0051:0.012]
	Coastlines	[-0.019:0.082]	[-0.0033:0.012]
[25th:75th]	Clear-sky over land	[-0.0029:0.0040]	[-0.00069:0.00087]
	Cloud over land	[-0.0016:0.0030]	[-0.00058:0.0012]
	Cloud over water	[-0.0032:0.011]	[-0.00090:0.0027]
	Coastline	[-0.0026:0.015]	[-0.00034:0.0027]